Materials Advances

ROYAL SOCIETY OF CHEMISTRY

PAPER

View Article Online
View Journal | View Issue

Cite this: *Mater. Adv.*, 2025, 6, 4499

Fluorescence switching *via* competitive ESIPT and spirolactam ring opening in a multifunctional rhodamine B probe for selective detection of Cu^{2+} and OCl^-: theoretical insights with anticancer and biosensor activity†

Vishnu S,[a] Avijit Kumar Das, *[a] Gouri Karan[b] and Sujata Maiti Choudhury[b]

A multifunctional ESIPT-based rhodamine-derived probe (**BHS**) was synthesized and developed as a colorimetric and fluorometric sensor for the selective detection of copper (Cu^{2+}) and hypochlorite (OCl^-) in aqueous solutions. Initially, **BHS** exhibits intense whitish blue fluorescence due to the active excited-state intramolecular proton transfer (ESIPT) mechanism within the molecule. However, upon interaction with Cu^{2+} and OCl^-, noticeable changes in absorption and fluorescence occur, attributed to the inhibition of ESIPT resulting from analyte binding with **BHS**, leading to spirolactam ring opening. Furthermore, significant Stokes shifts in absorption ($\Delta\lambda$ = 34 nm and 170 nm for Cu^{2+}, and 163 nm for OCl^-) and emission ($\Delta\lambda$ = 67 nm for both Cu^{2+} and OCl^-) further confirm this transformation. The spirolactam ring opening is induced by Cu^{2+} coordination, whereas for OCl^-, it is triggered by oxidative cleavage. To explore potential biological applications, fluorescence titration experiments were conducted to study the interactions of the **BHS**–Cu^{2+} complex with ct-DNA and the transport protein bovine serum albumin (BSA). Additionally, molecular docking studies were performed to assess these interactions, while DFT calculations were employed to optimize the structures of **BHS** and its Cu^{2+} complex. The fluorescence changes of **BHS** in the presence of Cu^{2+} and OCl^- in biological samples have been examined by the anticancer and biosensor activity of **BHS** in HCT-116 colorectal cancer cells.

Received 20th May 2025,
Accepted 23rd May 2025

DOI: 10.1039/d5ma00517e

rsc.li/materials-advances

1. Introduction

Metal ions and anions are essential for a variety of pathological and physiological functions, including catalysis, osmotic control, metabolism, and more. However, it is generally recognized that abnormalities in the concentrations of specific ions in organisms can have a negative impact on normal biological events.[1] In this respect, metal ion copper is a micronutrient that is necessary for humans, plants and animals. Copper stands in the third position of the most abundant trace metals in earth's crust, behind iron and zinc. Numerous physiological functions, including red blood cell production, and maintenance and healthy development of brain tissues, the heart, kidneys, and other organs, rely on copper(II) ions.[2,3] Research findings suggest that one of the variables raising the risk of coronary heart disease is copper misregulation. Furthermore, among the most prevalent contaminants, particularly in drinking water, Cu^{2+} in turn degrades water quality and causes a number of illnesses.[4] Additionally, a number of genetic and metabolic diseases in humans, including Parkinson's disease, Alzheimer's disease, Wilson's disease, obesity, diabetes, and others, are brought on by copper dysregulation.[5] The WHO states that the amount of copper ions in drinking water should not exceed more than 31.4 μM in order to safeguard human health.[6]

Similarly, one among the most common ROS-reactive oxygen species is hypochlorite (ClO^-). Endogenous hypochlorite is a physiologically significant ROS that is essential to many physiological and pathological processes.[7] It is primarily produced by the innate immune system's myeloperoxidase (MPO)-mediated peroxidation of hydrogen peroxide (H_2O_2) and chloride (Cl^-).[8] It has been demonstrated that an excess of hypochlorite can be harmful and result in conditions including cancer, atherosclerosis, rheumatoid arthritis, fibrillation, and asthma. Cell well-being is majorly dependent on the optimum concentration of

[a] Department of Chemistry, Christ University, Hosur Road, Bangalore, Karnataka, 560029, India. E-mail: avijitkumar.das@christuniversity.in
[b] Cancer Nanotherapeutics Laboratory, Biochemistry, Molecular Endocrinology, and Reproductive Physiology Division, Department of Human Physiology, Vidyasagar University, Midnapore-721 102, West Bengal, India

† Electronic supplementary information (ESI) available. See DOI: https://doi.org/10.1039/d5ma00517e

hypochlorite.[9] Hence, the development of methods for copper ion and hypochlorite detection has been of utmost importance in environmental and food nutritional fields.

Several techniques have been established for the detection of metallic cations, such as ion chromatography,[10] high-performance liquid chromatography,[11] voltammetry,[12] electrochemical,[13] and ICP-AES - inductively coupled plasma atomic emission spectrometry,[14] *etc.* Although these methods prove to be efficient, they still suffer from certain limitations, such as expensive procedures and instrumentation, complicated operational protocols, and excessive sample pretreatment.[15] In order to overcome these limitations, fluorescence chemosensors have attracted a lot of interest compared to alternative techniques due to their many benefits, which include ease of device manufacturing, low cost, excellent stability, and quick disposability.[16] Fluorescent chemosensors have the ability to selectively detect several chemical species including cations,[17] anions,[18] and other compounds, by altering their fluorescence properties. These chemosensors have been widely developed and utilized in the domains of chemistry, life science, environmental research, and materials science due to their high detection sensitivity, rapid analyte response, ease of handling, and ability to facilitate real-time analysis.[19] The rhodamine molecule is a notable example of an off–on type fluorescent probe among the known fluorescent compounds. First created in 1905 by Noelting and Dziewonsky, rhodamine is a class of xanthene-derived dye used in analytical research, initially used for colorimetric detection of a variety of substances, including zinc and silver.[20] Since then, rhodamine as a scaffold has gained vast significance in analyte detection *via* colorimetric and fluorometric paths owing to its unique characteristics, such as high quantum yields of fluorescence, large molar extinction coefficients, and both long emission and absorption wavelengths.[13] Rhodamine's structure includes a spirolactam ring, which can be observed in two structural forms. The ring opening is generally facilitated upon binding with cations, anions, and certain neutral molecules. While the ring closure spirolactam derivatives are nonfluorescent and colorless, opening of the spirolactam ring results in notable fluorescence changes and a noticeable brilliant pink color.[21] Despite the fact that organic optoelectronic materials have employed a variety of binding mechanisms, the ESIPT-excited-state intramolecular proton transfer phenomenon, a photo-induced proton transfer *via* an intramolecular hydrogen bond, is of great interest because of its exciting photochemical and photophysical applications.[22]

The ESIPT process, initially reported in the 1950s by Weller for salicylic acid, has been extensively studied since then for various applications. ESIPT fluorescence occurs when molecules have intramolecular hydrogen bonding between donors and acceptors. ESIPT involves a fast enol-to-keto phototautomerization ($k_{ESIPT} > 10^{12}$ s^{-1}) followed by a radiative decay and reverse proton transfer (RPT) to regenerate the enol form (Scheme 1a). Its significant Stokes shift improves efficiency and helps prevent fluorophores from self-absorbing.[23] Common ESIPT fluorophores include analogues of 2-(2′-hydroxyphenyl)-benzimidazole, benzoxazole, and benzothiazole, along with quinoline, benzophenones, flavones, anthraquinones, benzotriazoles, and others.[24] However, these ESIPT chromophores have rarely been coupled with rhodamine-based sensors for analyte detection (Scheme 1b).[25] Therefore, we have designed and synthesized a multifunctional ESIPT based fluorescent probe 3′,6′-bis(diethylamino)-2-((4-(diethylamino)-2-hydroxybenzylidene)-amino)spiro[isoindoline-1,9′-xanthen]-3-one (**BHS**) based on the Schiff base condensation reaction of rhodamine B hydrazide with 4-(diethylamino)salicylaldehyde derivatives for dual detection of cation Cu^{2+} and anion hypochlorite (OCl^-). Probe **BHS** has been characterized by NMR and mass spectroscopy (Fig. S1 and S2, ESI†).

2. Experimental section

2.1. Synthesis of rhodamine B hydrazide (compound 1)

The synthesis procedure for **compound 1** was adapted from Dujols *et al.*[26] The process involved a single-step reaction between rhodamine B and hydrazine hydrate in methanol (Scheme 2a). In particular, rhodamine B (0.8 g) was solubilized in 30 mL of methanol, followed by the addition of excess hydrazine hydrate (1 mL). TLC was used to track the reaction mixture's progress and the refluxing continued until the disappearance of the pink color. After the completion of the

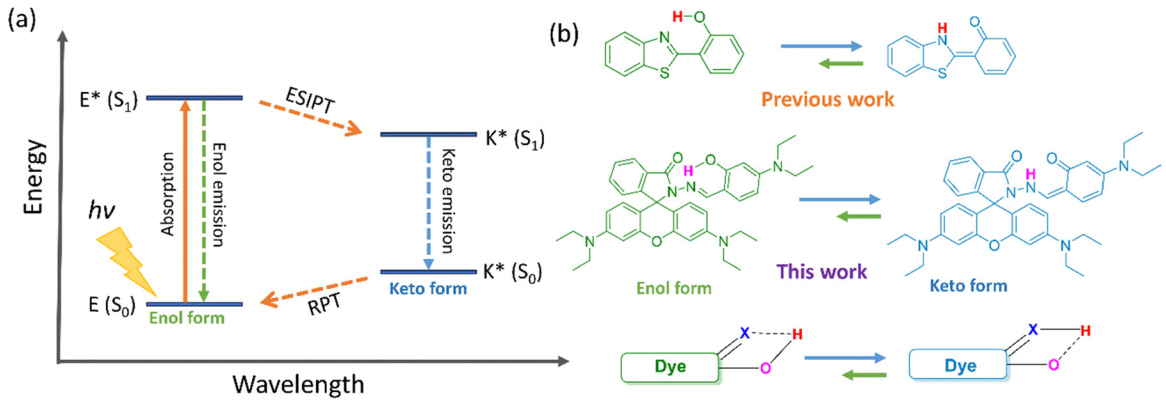

Scheme 1 (a) Diagrammatic representation of the ESIPT process. (b) Comparison of the ESIPT phenomenon with previous work and the current work.

Synthetic scheme:

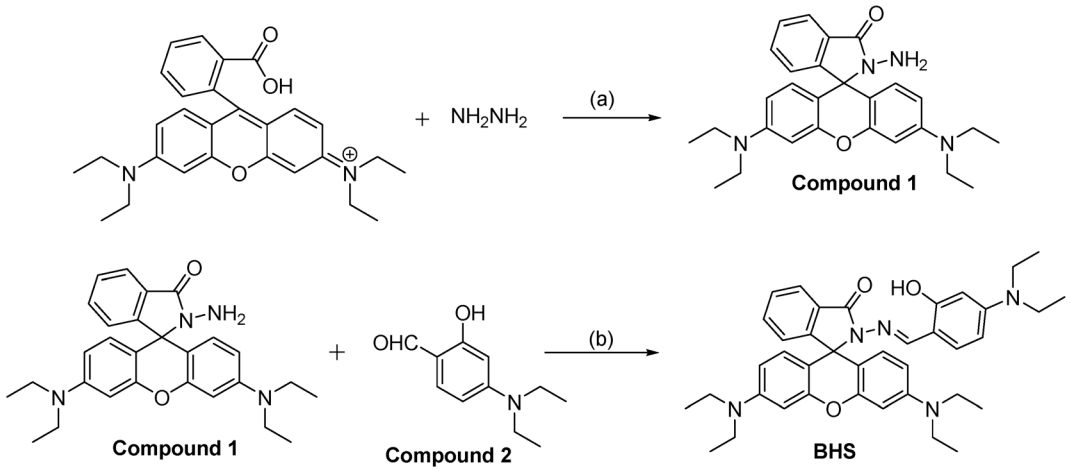

Scheme 2 (a) MeOH, reflux, overnight. (b) MeOH, rt, 24 h.

reaction, the mixture was transferred into ice-cold water and a solid pink color precipitated out. The precipitate was then filtered and left to dry. A solid product yielding a total of 0.54 g (68%) of **compound 1** was obtained.

2.2. Synthesis of BHS

The compound **BHS** was synthesized by condensation of rhodamine B hydrazide (**compound 1**) (236.2 mg, 0.5173 mmol) and 4-(diethylamino)salicylaldehyde (**compound 2**) (100 mg, 0.5175 mmol) in methanol (20 mL) and the mixture was stirred at room temperature for 24 h. The reaction progress was monitored *via* TLC. A yellow-colored product was filtered, followed by drying, and it was further recrystallized from ethyl acetate (Scheme 2b). Yield: 70 mg, 21%, Mp: 275 °C. ^{1}H NMR ($CDCl_3$, 400 MHz): δ (ppm): 10.94 (s, 1H, –OH), 9.18 (s, 1H, ═CH), 7.94 (t, 1H, J = 4 Hz), 7.49 (t, 2H, J = 3.6 Hz), 7.15 (t, 1H, J = 4 Hz), 6.19 (d, 1H, J = 8.4 Hz), 6.47 (q, 4H), 6.25 (q, 2H), 6.11 (d, 2H, J = 11.2), 3.31 (q, 12H), 1.41 (q, 18H). Mass (m/z): M^+ calculated for $C_{39}H_{45}N_5O_3$ is 631.35; found: 633.49 $(M + 2H)^+$. Elemental analysis: calculated value: C, 74.14; H, 7.18; N, 11.08. Observed value: C, 74.18; H, 7.17; N, 11.05.

3. Results and discussion

3.1. Binding study with Cu^{2+} and OCl^-

To gain insights into the sensing abilities of the synthesized probe **BHS**, emission and absorption studies were conducted with various analytes, including metal ions and anions. The colorimetric and fluorescence properties of **BHS** were analyzed with the addition of various metal ions, like Al^{3+}, Cd^{2+}, Fe^{2+}, Fe^{3+}, Cu^{2+}, Ni^{2+}, Pb^{2+}, Hg^{2+}, Co^{2+}, Mn^{2+}, and Zn^{2+}, in a CH_3CN-HEPES buffer (9 : 1, v/v, pH 7.4). The probe **BHS** initially produced an absorbance peak at 382 nm, which, over the addition of Cu^{2+}, exhibited a bathochromic shift resulting in the generation of two strong absorption signals at 416 nm ($\Delta\lambda$ = 34 nm) and 552 nm ($\Delta\lambda$ = 170 nm) along with an isobestic point at 402 nm. This large spectral shift indicates the presence of the ESIPT phenomenon within the molecule. Incremental addition of Cu^{2+} led to a gradual increase in the absorption peak at 552 nm, followed by a noticeable naked-eye color transition, generating pink color from colorless (Fig. 1a). The absorbance of **BHS** changes with the concentration of Cu^{2+} up to the saturation level (Fig. 1b). A linear increase in Cu^{2+} concentration results in a corresponding linear rise in absorbance, which is attributed to the observed color change. The emission spectrum of **BHS** alone produced a strong signal at 509 nm when excited at 400 nm. However, after the introduction of Cu^{2+} into the probe solution, a significant decrease in fluorescence intensity at 509 nm was observed along with the emergence of a red-shifted emission signal at 576 nm ($\Delta\lambda$ = 67 nm) at a high concentration of Cu^{2+}, which corresponds to the emission signal appearance upon the spirolactam ring opening of rhodamine. Attributed to the **BHS**–Cu^{2+} binding, the fluorescence intensity gradually decreases with increasing concentrations of Cu^{2+} (Fig. 1d).

Similarly, the UV-vis and fluorescence behavior of **BHS** was studied with the addition of several anions, such as Br^-, $C_2O_4^-$, CH_3COO^-, Cl^-, F^-, I^-, H_2O_2, NO_2^-, NO_3^-, OCl^-, and SO_4^{2}, in CH_3CN-HEPES buffer (9 : 1, v/v, pH 7.4). The probe **BHS** itself exhibited a single distinct absorption maximum at 382 nm without the addition of any analytes. However, on exposure to OCl^-, a new red-shifted absorption signal emerged at 545 nm ($\Delta\lambda$ = 163 nm), which was gradually enhanced with increasing concentrations of OCl^- (Fig. 2a and b). This transition was accompanied by a prominent, visually detectable color change from colorless to pink. As a result, a linear increase in absorbance was observed with increasing OCl^- concentrations (Fig. 2b). In the fluorescence spectra, the probe **BHS** initially exhibited a strong whitish blue fluorescence with a prominent emission peak at 509 nm. Upon the addition of OCl^-, the emission signal exhibited a red shift ($\Delta\lambda$ = 67 nm) to 576 nm from 509 nm followed by the decrease of the emission intensity at 576 nm with the appearance of weak red fluorescence (Fig. 2c and d). The significant Stokes shift in the emission spectra also

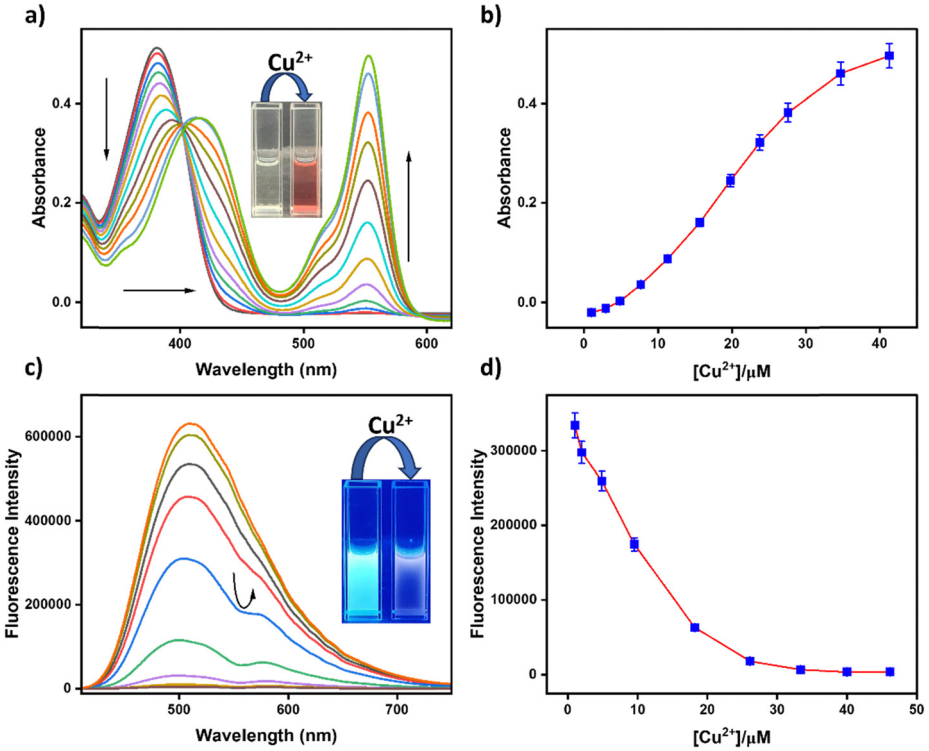

Fig. 1 (a) and (c) Colorimetric and fluorometric response of **BHS** (c = 2 × 10^{-5} M) with the addition of Cu^{2+} (c = 2 × 10^{-4} M, 10 equiv.). (b) and (d) Changes in concentrations *vs.* intensity of **BHS** with Cu^{2+} in absorption and emission titration spectra, respectively (λ_{em} = 576 nm).

suggests the occurrence of the ESIPT phenomenon within the molecule.

3.2. Interference study

Interference analysis using colorimetric and fluorometric methods was performed to evaluate the selectivity of **BHS** toward Cu^{2+} by testing various metal ions, including Al^{3+}, Cd^{2+}, Fe^{2+}, Fe^{3+}, Hg^{2+}, Mn^{2+}, Ni^{2+}, Co^{2+}, Pb^{2+}, and Zn^{2+}, in CH_3CN-HEPES buffer (9 : 1, v/v, pH 7.4). The probe solution exhibited no notable absorption peak at 552 nm in the presence of different metal ions. Slight interference from Fe^{2+} was observed in the absorption spectra, indicated by the appearance of a pale pink color visible to the naked eye (Fig. 3a and b). However, upon the addition of Cu^{2+}, a prominent signal appeared at 552 nm, attributed to the formation of a distinct pink color from the initially colorless probe solution. The naked eye visible color change appeared selectively in the presence of Cu^{2+} (Fig. 3a) with the appearance of the corresponding strong UV-vis absorption signal (Fig. 3b), while Fig. 3c presents a bar graph of the absorption intensities, with the red bar representing the solution containing Cu^{2+}.

Similarly, fluorometric titration analysis revealed that no metal ion induced significant changes in the probe solution, except for Cu^{2+}. This metal ion Cu^{2+}, along with displaying a prominent quenching of fluorescence intensity at 509 nm, produced a secondary signal at 576 nm, which can be attributed to the binding interaction between **BHS** and Cu^{2+} (Fig. 4). The fluorescence quenching phenomena pave the way to the emergence of new fluorescence, as observed under a UV chamber (Fig. 4a). The emission spectrum of **BHS** with various metals ions has been shown in the interference study, wherein the signal of emission at 509 nm was unaffected with the presence of any other interfering cations except for Cu^{2+} but minor interference from Co^{2+} was detected in the fluorescence spectra (Fig. 4b). While bar graph representation displays the same observation on exposure to several interfering metal ions and the lower intensity red bar indicates the emission response of **BHS** in the presence of Cu^{2+} at 509 nm (Fig. 4c).

Similarly, the interference analysis of **BHS** with various anions, including Br^-, $C_2O_4^{2-}$, CH_3COO^-, Cl^-, F^-, I^-, $H_2O_2^-$, NO_2^-, NO_3^- and SO_4^{2-}, was conducted in CH_3CN-HEPES buffer (9 : 1, v/v, pH 7.4). Only exposure to OCl^- produced significant changes in absorbance and emission intensities at 545 nm and 576 nm, respectively. The absorption spectrum displayed a distinctive peak at 545 nm, while the fluorescence spectrum exhibited a new, selective signal at 576 nm exclusively with OCl^-. No notable changes in absorbance or emission were observed in the presence of several other anions (Fig. 5 and 6). In the bar graph depiction of the same, the selective behavior of **BHS** toward OCl^- is highlighted with a pink bar of higher intensity compared to the lower-intensity yellow bars for other anions in the absorption study (Fig. 5c). Similarly, in the fluorescence study, a lower-intensity bar (pink) represents OCl^-, contrasting with higher-intensity bars (yellow) for other anions (Fig. 6c). All these results demonstrate the selective interaction of **BHS** with Cu^{2+} and OCl^- against all the interfering metal ions and anions.

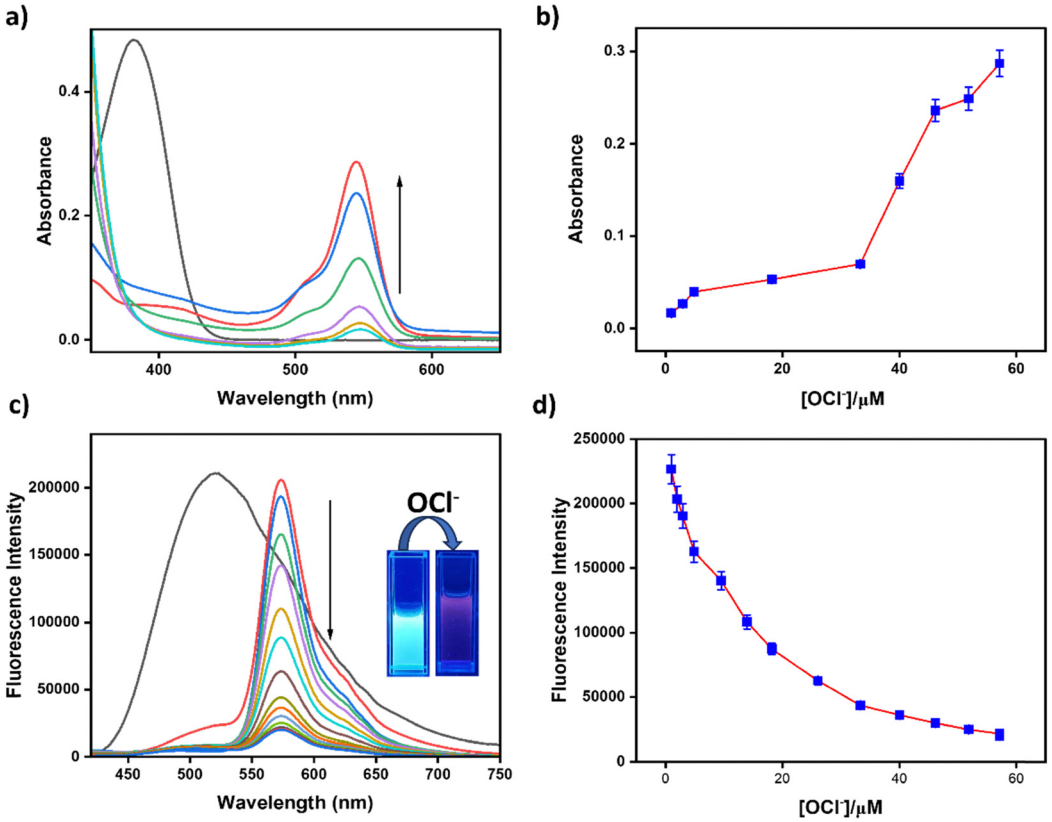

Fig. 2 (a) and (c) Absorption and emission titration signals of **BHS** (c = 2 × 10^{-5} M) with the addition of OCl^- (c = 2 × 10^{-4} M, 10 equiv.). (b) and (d) Concentrations *vs.* intensity variations of **BHS** with OCl^- in colorimetric and fluorometric titration spectra, respectively (λ_{em} = 576 nm).

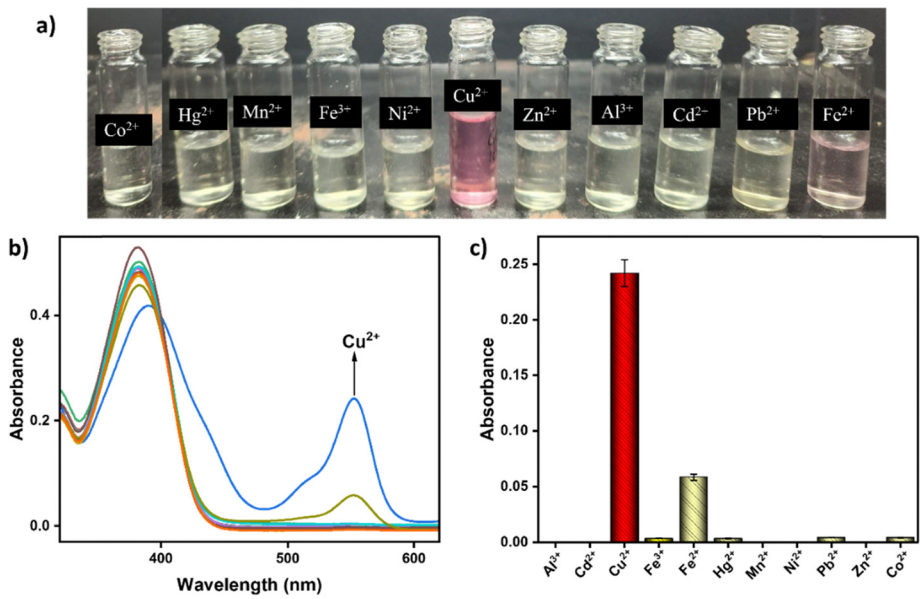

Fig. 3 (a) Naked eye colour changes of probe **BHS** with several metal ions. (b) Colorimetric behaviour of **BHS** on exposure to diverse metal ions (10 equiv.) in CH_3CN–aqueous HEPES buffer solution (9/1, v/v, pH = 7.4). (c) Absorption intensity changes of the sensor **BHS** upon introduction of the interfering metal ions (c = 2 × 10^{-4} M, 10 equiv.).

3.3. Competition study

Furthermore, a competition study was conducted to analyze the selective binding abilities of **BHS** toward Cu^{2+} and OCl^- against several other competing cations and anions, respectively, in CH_3CN-HEPES buffer (9 : 1, v/v, pH 7.4). The absorption spectra demonstrate the selectivity of **BHS** for Cu^{2+} (red bars) and OCl^-

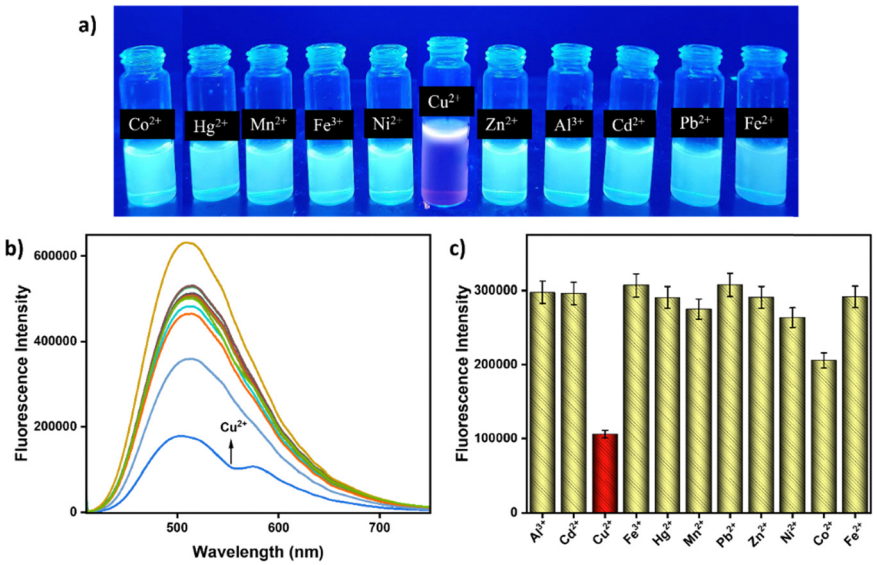

Fig. 4 (a) Fluorescent properties of probe **BHS** with various cations under UV light. (b) Fluorescence signal of **BHS** on the addition of various cations (10 equiv.) in CH_3CN–aqueous HEPES buffer solution (9/1, v/v, pH = 7.4). (c) Changes in fluorescence intensity of the sensor **BHS** with the addition of other interfering cations ($c = 2 \times 10^{-4}$ M, 10 equiv.).

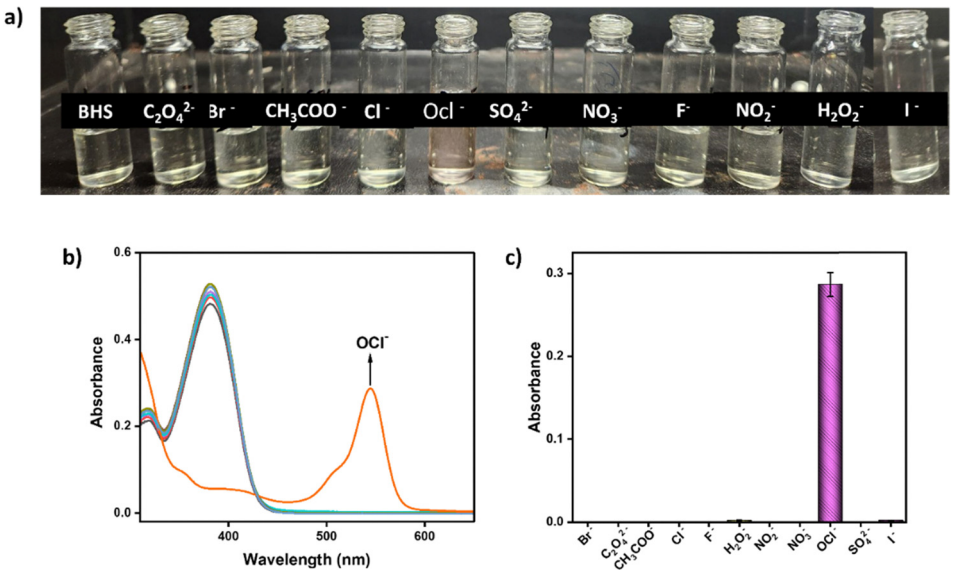

Fig. 5 (a) The changes of naked eye color of the probe **BHS** with several anions. (b) Absorption behaviour of **BHS** upon addition of several anions (10 equiv.) in CH_3CN–aqueous HEPES buffer solution (9/1, v/v, pH = 7.4). (c) Absorption intensity changes of the probe **BHS** upon the addition of interfering anions ($c = 2 \times 10^{-4}$ M, 10 equiv.).

(pink bars), with the emergence of prominent peaks at 552 nm and 545 nm, respectively, even in a competing ionic environment (Fig. 7a and b). This indicates minimal competition effects on the efficiency of **BHS** towards selective detection of Cu^{2+} and OCl^-. Furthermore, the fluorescence titrations showed that Cu^{2+} and OCl^- selectively quenched the fluorescence of **BHS**. The high fluorescence intensity (yellow bars) represents the signal of **BHS** with individual ions, whereas, in the presence of Cu^{2+} (red bars) and OCl^- (pink bars), a notable decrease in fluorescence intensity at 576 nm was observed, confirming the selective detection of target analytes. These results further assert the strong selectivity of **BHS** for Cu^{2+} and OCl^- (Fig. 7c and d).

On the basis of the fluorometric studies of **BHS** with Cu^{2+} and OCl^-, the limits of detection of the probe **BHS** for Cu^{2+} and OCl^- were determined as 6.3 μM and 8.21 μM, respectively, utilizing the formula DL = $K \times Sb_1/S$, where $K = 3$, Sb_1 is the standard deviation of the blank solution, and S is the slope of the calibration curve (Fig. S5 and S6, ESI†).[27] At 552 nm, the molar absorption coefficients for **BHS** and **BHS**–Cu^{2+} were calculated as

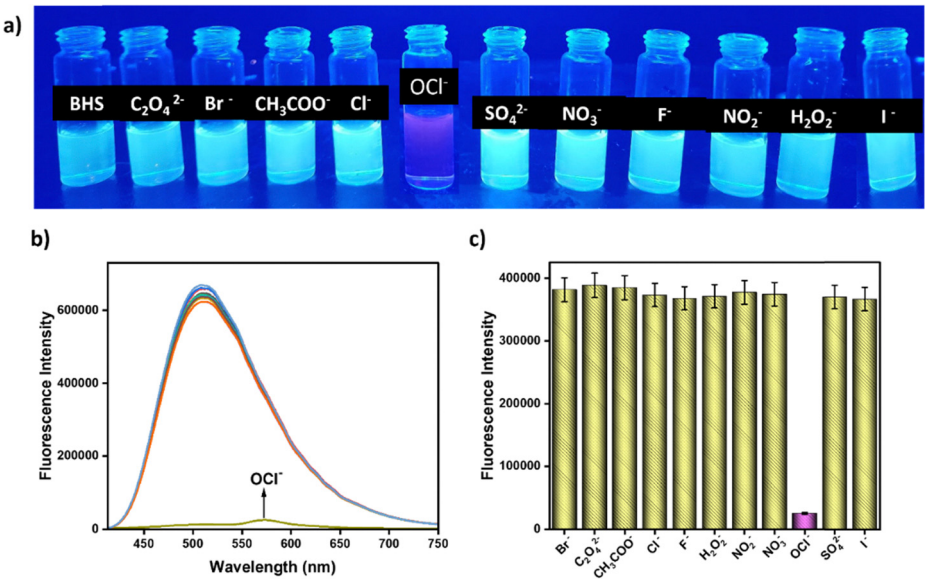

Fig. 6 (a) Fluorescent properties of ligand **BHS** with different anions under UV light. (b) The fluorescence spectra of **BHS** with the addition of several anions (10 equiv.) in CH_3CN–aqueous HEPES buffer solution (9/1, v/v, pH = 7.4). (c) Changes of fluorescence intensity of the sensor **BHS** with the addition of various interfering anions ($c = 2 \times 10^{-4}$ M, 10 equiv.).

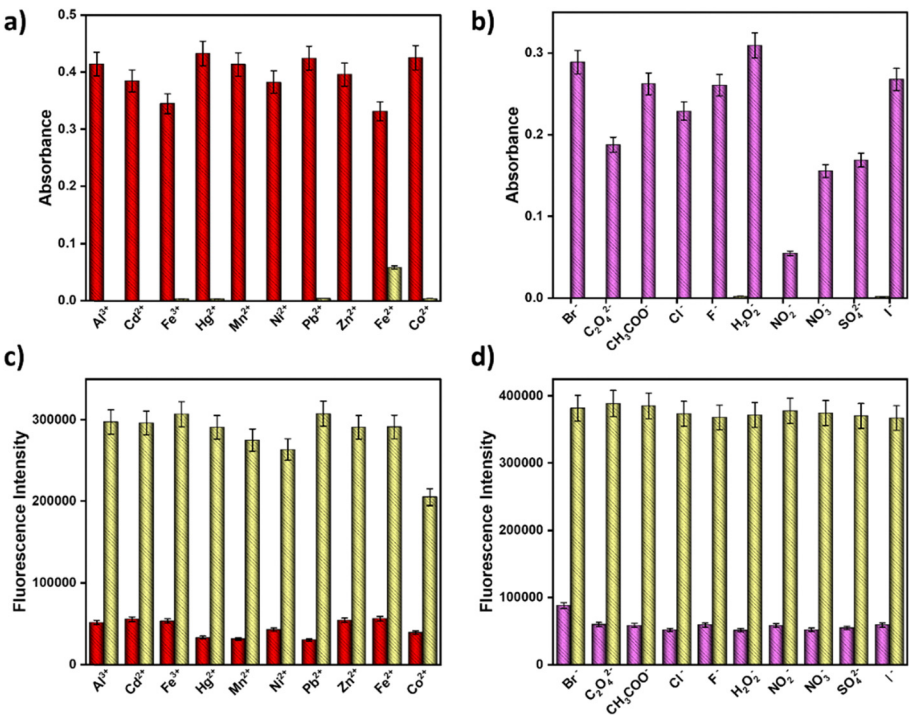

Fig. 7 (a) and (c) Changes in colorimetric and fluorometric spectra of **BHS** ($c = 2 \times 10^{-5}$ M) upon the addition of several metal ions ($c = 2 \times 10^{-4}$ M, 10 equiv.) (golden bars); changes in emission behaviour of these interfering metal ion signals against the addition of Cu^{2+} (red bars). (b) and (d) Change in colorimetric and fluorometric spectra of **BHS** ($c = 2 \times 10^{-5}$ M) upon addition of several anions ($c = 2 \times 10^{-4}$ M, 10 equiv.) (golden bars); changes in emission behaviour of these interfering anions against the addition of OCl^- (pink bars).

10.57×10^3 mol^{-1}-liter-cm^{-1} and 2.48×10^3 mol^{-1}-liter-cm^{-1}. Through the Jobs plot analysis, the 1 : 1 binding stoichiometry for **BHS**–Cu^{2+} complexation was verified and from the fluorescence titration experiment, the association constant (K_a) of **BHS** with Cu^{2+} was calculated as 2.7×10^5 M^{-1} (error < 10%) (Fig. S9, ESI†).[28,29] To further evaluate the probe's stability and sensing capabilities across different pH environments, UV-vis experiments were conducted. Notably, the sensor **BHS** exhibited an

intense naked-eye-visible color in strongly acidic conditions, accompanied by a strong absorption signal at 552 nm, while no response was observed in neutral or basic media. This indicates that the spirolactam ring opens in acidic environments without the addition of metal ions, whereas it remains stable in neutral and basic media. However, in the presence of Cu^{2+}, the spirolactam ring also opens under neutral and basic conditions (Fig. S11, ESI†). Therefore, to simulate physiological conditions, the sensing behavior of **BHS** with Cu^{2+} and OCl^- was studied at pH 7.4 using HEPES buffer.

3.4. Reversibility study

A fluorometric analysis was performed to assess the reversibility of the binding interaction between **BHS** and Cu^{2+}, providing further insights into the binding properties of **BHS** with Cu^{2+}. The intensity of the fluorescence gradually increased upon incremental addition of H_2S to the **BHS**–Cu^{2+} complex, indicating the reversible binding behavior of **BHS** with Cu^{2+} (Fig. 8). The notable fluorescence enhancement suggests that H_2S extracts Cu^{2+} from the **BHS**–Cu^{2+} complex, releasing the free probe **BHS** and confirming its reversible metal ion binding.

3.5. Probable binding mode

Without the presence of analytes, the ligand **BHS** alone exhibits strong whitish blue fluorescence due to the conversion of the enol intermediate to the keto form through an ultrafast photo-induced tautomerization process *via* excited-state intramolecular proton transfer (ESIPT). This process involves the transfer of a proton from the acidic hydroxyl group to the basic imine nitrogen, facilitated by the formation of a six-membered transition state (pathway a, Scheme 3). As a result, **BHS** shows a strong absorbance signal at 382 nm and emission signal at 509 nm with notable Stokes shifts at about 127 nm. Moreover, large spectral shifts of absorption ($\Delta\lambda$ = 34 nm and 170 nm for Cu^{2+} and 163 nm for OCl^-) and emission signals ($\Delta\lambda$ = 67 nm for Cu^{2+} and OCl^-) of **BHS** on binding with Cu^{2+} and OCl^- suggest the occurrence of the ESIPT phenomenon within the molecule.[30] But, the changes in absorption and fluorescence upon exposure to Cu^{2+} and OCl^- are attributed to the suppression of ESIPT due to analyte binding with **BHS**, followed by spirolactam ring opening. For Cu^{2+}, this occurs through metal ion coordination, while for OCl^-, it is driven by oxidative cleavage. During the interaction, a ring strain is influenced within the molecule due to the high Lewis acid strength of copper and its coordination with nitrogen and oxygen donor centers in **BHS**. The Cu^{2+} chelation with the rhodamine-linked derivative **BHS** triggers a chelation-enhanced fluorescence (CHEF) ''off–on'' colorimetric and fluorometric response (pathway b, Scheme 3). This transformation involves the translation of the colorless, non-fluorescent spirolactam structure **BHS** to the ring-open form, **BHS1**, which exhibits strong fluorescence and pink color. Spectroscopic analyses, including mass spectrometry and DFT studies, support this mechanistic transformation. The **BHS1** and Cu^{2+} complex formation was confirmed by the appearance of a mass peak at m/z = 735.50 (Fig. S3, ESI†), corresponding to [**BHS**–Cu^{2+}–CH_3CN]$^+$ (Fig. S4, ESI†). A 1 : 1 binding stoichiometry has been confirmed through the Job's plot analysis and further corroborated by DFT analysis (Fig. S8, ESI†). The opening of the spirolactam ring of the rhodamine derivative is responsible for the changes of absorption and emission color of **BHS** upon the addition of OCl^-. Coordination of metal ions such as Cu^{2+} with the rhodamine moiety usually results in ring opening without any loss of groups from the binding site of the rhodamine derivative. Nevertheless, in the presence of water, OCl^- oxidizes the hydrazide group of **BHS**, leading to the formation of pink-colored, red fluorescent rhodamine-B itself (**BHS2**) (pathway c, Scheme 3). This transformation is confirmed by the presence of a mass peak at m/z = 444.02, corresponding to mass of rhodamine-B (Fig. S4, ESI†).

3.6. Dipstick method

To analyze the real-time applicability of the probe, test strips were created by initially treating TLC plates with the synthesized receptor solution of **BHS** ($c = 2 \times 10^{-5}$ M). Furthermore, upon exposure of analytes OCl^- and Cu^{2+} to the test kits that had been pre-treated with the **BHS** probe, significant color changes were observed attributed to the detection capabilities of the probe (Fig. 9). These test strips, often referred to as dipsticks, have proved efficacy in delivering prompt qualitative results without requiring any kind of complex instrumental examination.

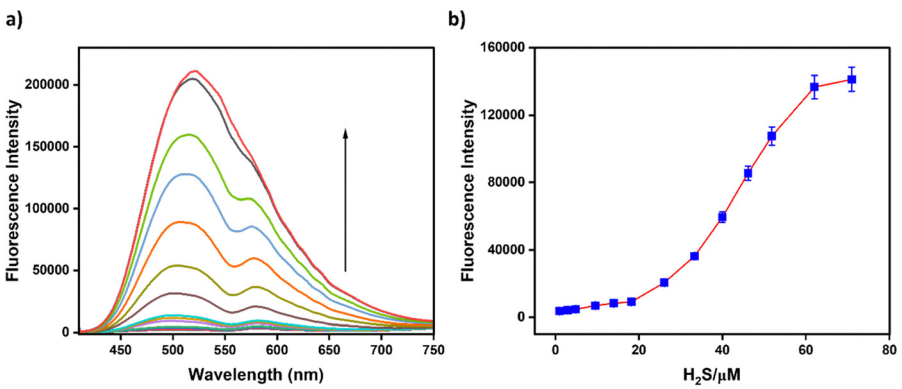

Fig. 8 (a) Emission behaviour of **BHS**–Cu^{2+} ($c = 2 \times 10^{-5}$ M) with the addition of H_2S solution ($c = 2 \times 10^{-4}$ M). (b) Emission intensity changes of the **BHS**–Cu^{2+} complex as a function of the H_2S concentration.

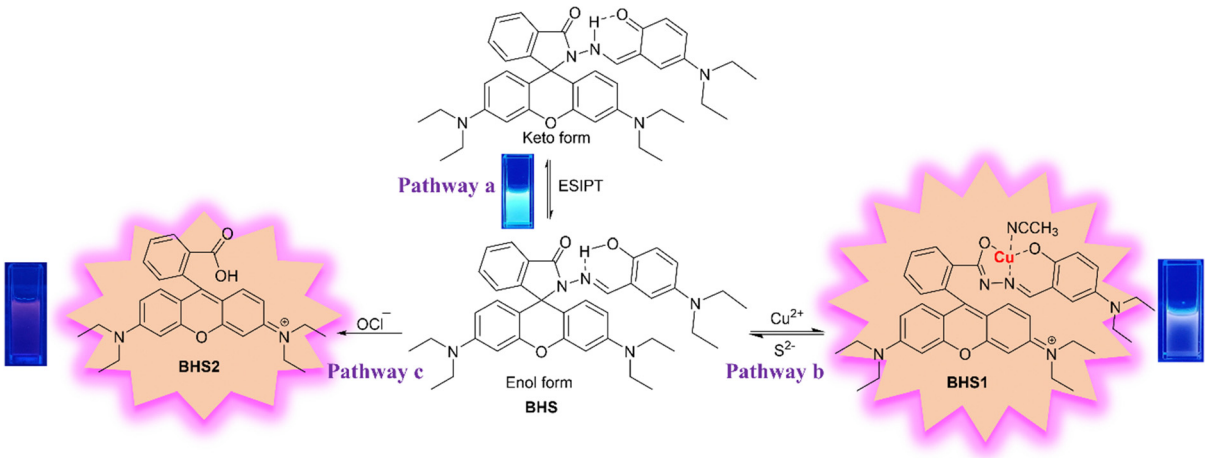

Scheme 3 Plausible binding of **BHS** with Cu^{2+} and OCl^- in the solution phase.

Fig. 9 Color changes of the **BHS**-treated TLC plates ($c = 2 \times 10^{-5}$ M) with an exposure to Cu^{2+} and OCl^- ($c = 2 \times 10^{-4}$ M).

3.7. Biological applications

3.7.1. DNA binding study. Fluorometric analysis was performed in order to evaluate the binding abilities of the metal–ligand complex along with duplex ct-DNA in a buffer medium of Tris–HCl (pH 7.2). The fluorescence signal corresponding to the **BHS**–Cu^{2+} complex exhibited quenching upon progressive addition of ct-DNA (Fig. 10a and b). The gradual reduction in fluorescence intensity at 576 nm over increasing additions of ct-DNA is attributed to the binding interaction between the metal–ligand complex and ct-DNA. Generally, upon binding with metal ions, the **BHS**–Cu^{2+} complex adopts a more rigid and sterically constrained structure, which hinders its ability to intercalate between the tightly packed DNA base pairs. Instead, it predominantly associates with the DNA grooves, especially the minor groove, where it can establish hydrogen bonding, van der Waals interactions, and electrostatic attractions with the DNA backbone. These interactions are more energetically favorable and accessible for the rhodamine–metal complex, resulting in groove binding rather than intercalation.[31] The detection limit for the fluorometric measurements of the DNA binding studies was determined to be 13.15 μM (Fig. S7a, ESI†). Based on the fluorometric experiments, the binding constant (K_b) of **BHS**–Cu^{2+} towards ct-DNA was calculated as 9.2×10^4 M^{-1} using a non-linear binding isotherm (Fig. S10a, ESI†).

3.7.2. Protein binding study. Furthermore, the probe **BHS** was analyzed for its binding capability towards bovine serum albumin (BSA) in a buffer medium of Tris–HCl (pH 7.2) using fluorescence titration studies. The emission spectrum of the **BHS**–Cu^{2+} metal–ligand complex exhibited two distinctive peaks: a relatively low-intensity signal at 463 nm and a higher-intensity signal at 576 nm (Fig. 10c). Interestingly, upon the serial addition of BSA to the complex, the fluorescence titration resulted in a ratiometric peak; the peak intensity at 463 nm progressively enhanced, whereas the higher-intensity peak at 576 nm displayed gradual quenching. The detection limit for the protein-binding study was calculated to be 23.08 μM using fluorometric analysis (Fig. S7b, ESI†) and based on a non-linear fluorometric binding isotherm, the binding constant (K_b) of the **BHS**–Cu^{2+} complex with BSA was determined to be 5.9×10^4 M^{-1} (Fig. S10b, ESI†).

3.7.3. *In vitro* cytotoxicity study on HCT-116 cells by MTT assay. Dose-dependent cytotoxicity of **BHS** was determined against HCT-116 colorectal cancer cells by the MTT assay. Soluble tetrazolium salt (yellow) is converted to purple formazan crystals by viable cells.[32] Based on this principle, it was found that **BHS** was able to produce significant toxicity in HCT-116 cells. The IC_{50} dose of 115.48 μM was calculated from the dose-effect curve, where cell viability was reduced to 50% of the control population. At the highest concentration dose of 250 μM, cell viability was reduced up to 27.29% (Fig. 11), which strongly denotes the potent anticancer activity of **BHS** against HCT-116 cells.

3.7.4. Fluorescence imaging study. The fluorescence activity of ligand **BHS** in the presence of sensing analytes copper (Cu^{2+}) and hypochlorite (OCl^-) was studied in the HCT-116 colorectal cancer cell line. Significant fluorescence shifting from 500 nm to 580 nm wavelength in the presence of analytes was denoted as efficient sensitivity of **BHS** for Cu^{2+} and OCl^- detection in biological samples. HCT-116 cells showed prominent emission of blue fluorescence near the 500 nm region, after 6 hours incubation with **BHS**, indicating endocytosis-mediated internalization of **BHS** in the cell cytoplasm. On the other hand, after further incubation with exogenous copper (Cu^{2+}) and hypochlorite (OCl^-), a significant reduction in blue fluorescence intensity was observed in the HCT-116 cells.

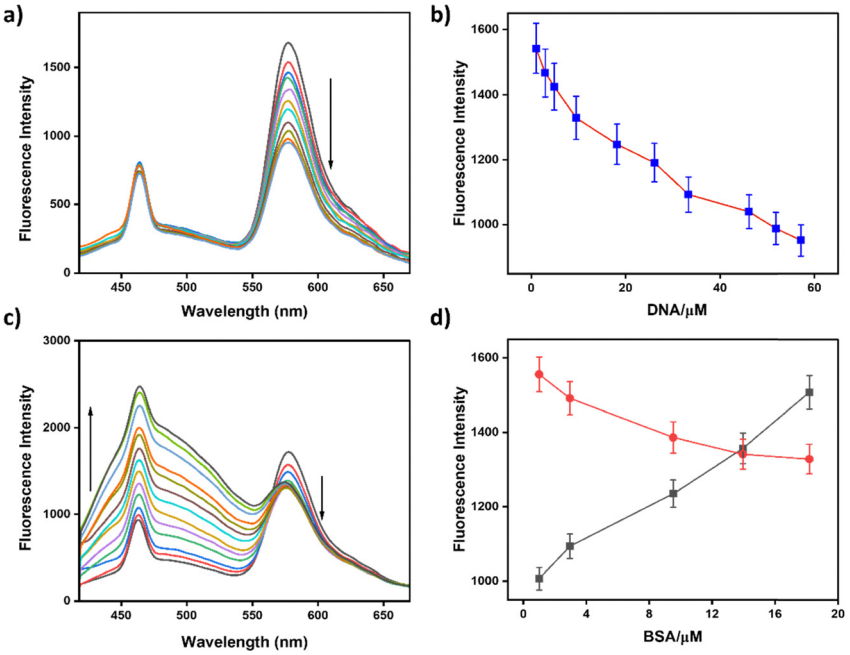

Fig. 10 Emission spectra of the **BHS**–Cu^{2+} complex (c = 2.0 × 10^{-5} M) over serial increments of (a) ct-DNA (c = 2 mM in base pairs) and (c) BSA (c = 7.4 μM) both in a buffer medium of Tris–HCl (pH 7.2), respectively. Changes in emission intensity of the complex (λ_{em} = 576 nm) with respect to (b) ct-DNA and (d) BSA concentrations.

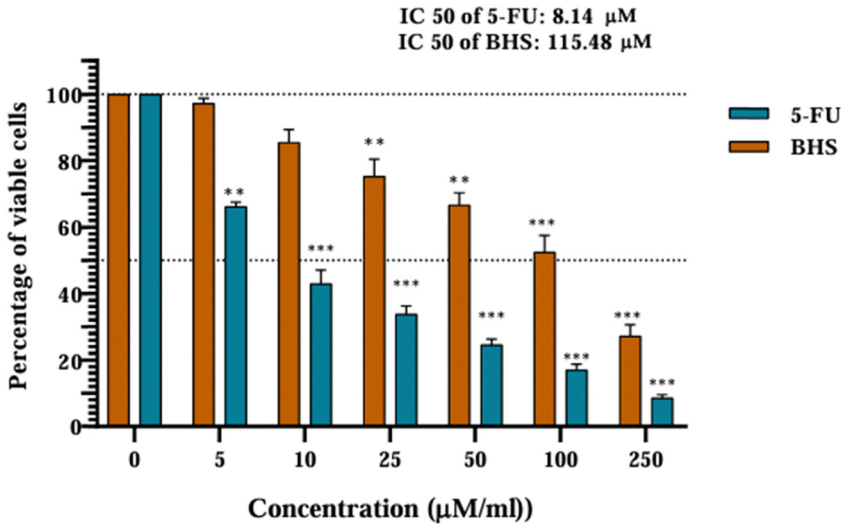

Fig. 11 A bar diagram of HCT-116 cell viability at different dosage concentrations of **BHS**. The calculated IC_{50} values of **BHS** and 5-FU were 115.48 and 8.14 μM, respectively. Data are presented as mean ± SEM of three independent experiments. '**' and '***' represent significant difference in cell viability compared to control HCT-116 cells at $p < 0.01$, $p < 0.001$, respectively.

However, red fluorescence emission was more prominent in the 580–600 nm region after Cu^{2+} and OCl^- treatment (Fig. 12). The data indicate a shift in fluorescence pattern from **BHS** from blue to red due to the formation of the ligand-analyte complex and alteration in electron transition.

3.8. Theoretical applications

3.8.1. DFT study. In order to elucidate the coordination chemistry of Cu^{2+}-**BHS**, structural optimizations using the density functional theory (DFT) method for both **BHS** and its Cu-complex were conducted at the B3LYP level (Fig. 13a). Initially the basis set 6-31G(d,p) was applied for the simple receptor (**BHS**), while the basis set LANL2DZ was employed for the Cu^{2+} complex. The Gaussian 09 software package was used to perform the calculations. Additionally, the spatial distribution of electron clouds was analyzed, and the orbital energies of the HOMO (highest occupied molecular orbital) and LUMO (lowest unoccupied molecular orbital) for both probe and its

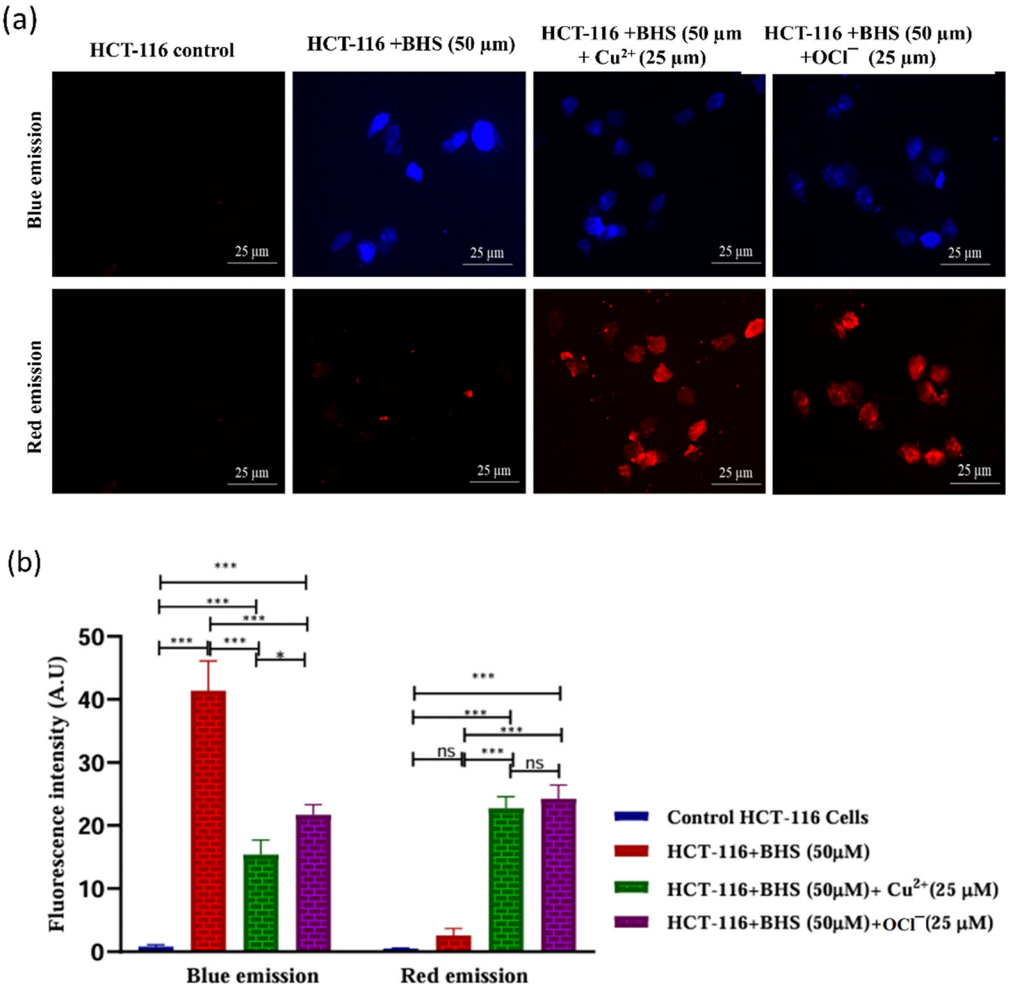

Fig. 12 (a) A fluorescence imaging study of HCT-116 colorectal carcinoma cells after the respective treatment strategy. HCT-116 cells treated with **BHS** showed significant blue fluorescence intensity at 500 nm wavelength, while significant ($p < 0.001$) red fluorescence emission near the 580–600 nm region was observed after incubation with exogenous Cu^{2+} and hypochlorite (OCl^-) analytes. **BHS**-treated cells showed negligible red fluorescence emission due to the intracellular low concentration of cuprous and hypochlorite ions. The images (magnification 400×) were captured by a fluorescence microscope (Leica DFC 295, Germany) using UV and green excitation filters. (b) The bar diagram represents relative fluorescence intensity expressed as mean ± SEM of three independent experiments. '*', '**', and '***' represent significant difference in cell viability compared to control HCT-116 cells at $p < 0.05$, $p < 0.01$, and $p < 0.001$, respectively.

metal-complex were computed. The HOMO in **BHS** was analyzed to be primarily localized within the spirolactam ring, whereas the LUMO was analyzed to be extended across the molecule (Fig. 13c). These findings imply that the opening of the spirolactam ring could have enhanced coordination involving the ionophore carbonyl oxygen, the oxygen of diethyl amino salicylaldehyde, and Cu^{2+}. Cu^{2+} coordinates with **BHS** through four coordination sites, including one nitrogen from the hydrazide group, two oxygen atoms from the carbonyl and hydroxyl groups of salicylaldehyde, and a single nitrogen from the acetonitrile solvent, adopting a square planar geometry according to the optimized structure of the **BHS**–Cu^{2+} complex. The calculated Cu–O bond lengths for the phenolic and hydrazide moieties were 1.99 Å and 2.09 Å, respectively, while the Cu–N bond lengths for the acetonitrile and hydrazone nitrogen atoms were 1.89 Å and 1.96 Å, respectively. The bond angles involving the imine nitrogen, Cu, phenolic oxygen, and hydrazide oxygen were determined to be 88.84° and 83.12°, while those involving the acetonitrile nitrogen, Cu, phenolic oxygen, and hydrazide oxygen were 91.15° and 96.87° (Fig. 13b).

On further analysis of the metal-complex it was found that, the π-electrons in the HOMO were predominantly confined near the metal center, while the LUMO was localized to the xanthene moiety. Following this the energy gap calculations were performed, wherein the gap between the HOMO (−4.650 eV) and LUMO (−0.957 eV) for **BHS** was calculated as 3.69 eV, whereas for the **BHS**–Cu complex, the energy gap was increased to 6.42 eV (HOMO = −6.901 eV, LUMO = −0.476 eV). From the TD-DFT study of the **BHS**–Cu complex, one of the experimental absorption signals appeared at 416 nm, which is so close to the theoretical TD-DFT calculated absorbance that appeared at 413.83 nm for S0 to S5 transition (energy: 2.996 eV, $f = 0.0015$).

3.8.2. *In silico* molecular docking studies. The molecular docking analysis was utilized to further explore the binding

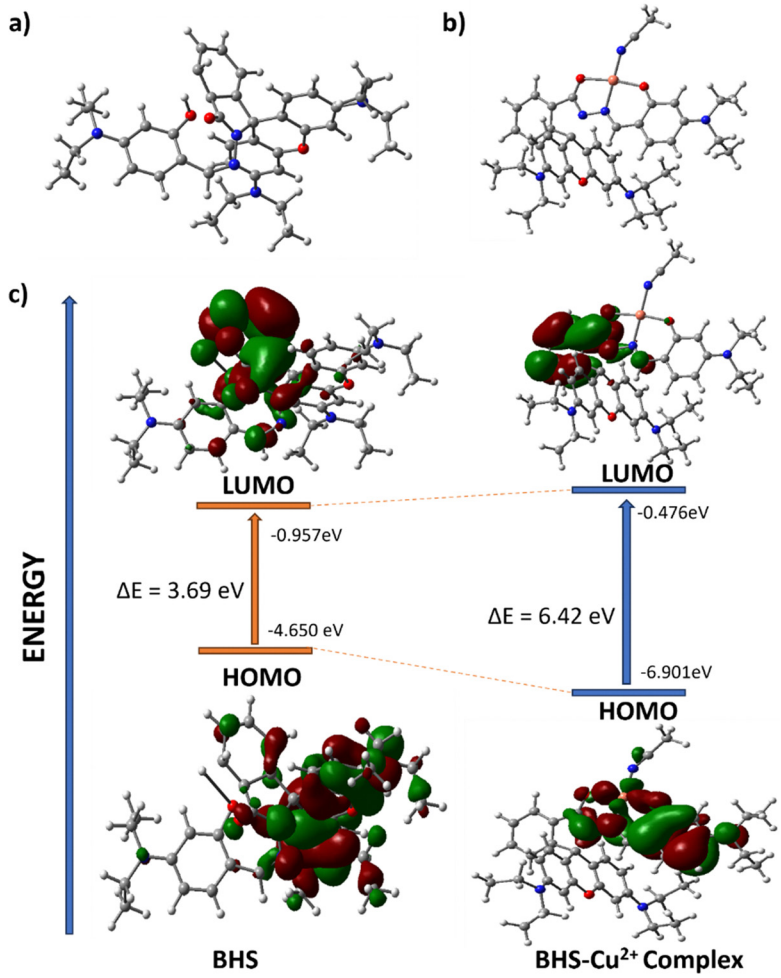

Fig. 13 Optimized geometrical molecular structure of both (a) **BHS** and (b) **BHS**–Cu^{2+} complex. (c) Frontier molecular orbital and the energy differences of the **BHS** and **BHS**–Cu^{2+} complex.

interactions of the **BHS**–Cu^{2+} complex with the ct-DNA and BSA protein. It is a technique that has been widely proven to be effective in predicting the possible binding site and the affinity of metal complexes with biomolecules, such as DNA and proteins.[32]

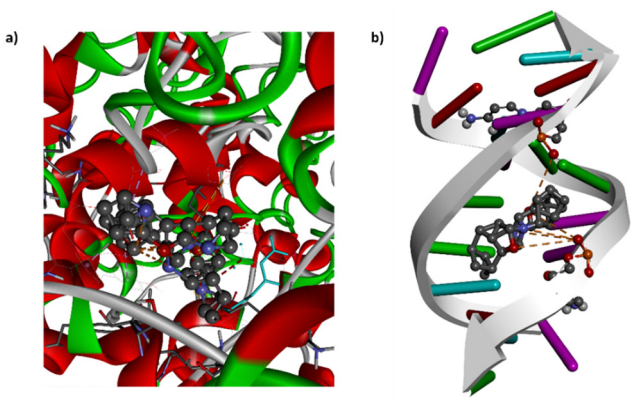

Fig. 14 Plausible binding mechanisms of the **BHS**–Cu^{2+} metal complex with (a) BSA and (b) ct-DNA complexes, respectively, in ribbon view.

This molecular docking analysis was performed with the Autodock Vina application (Fig. 14). The **BHS**–Cu^{2+} complex exhibited strong binding with the BSA protein (Fig. 14a) through amino acid residues such as GLU125, LYS136, ARG185, PHE133, TYR137, PRO117, LEU122 and others with a binding affinity of -19.6 kcal mol^{-1}. Similarly, the molecular docking study of the of **BHS**–Cu^{2+} complex with ct-DNA also helped in calculating the binding affinity of the ligand interaction with the DNA double helix to be -11.5 kcal mol^{-1} (Fig. 14b). These interactions between the metal complex and the double helix DNA molecule were established through cytosine [Cyt7, Cyt16, Cyt17], adenosine [Ade8], thymidine [Thy9], and guanosine [Gua14, Gua15] nucleotides. On analysing the above-mentioned docking results, we can conclude that, the **BHS**–Cu^{2+} complex has been established to possess a greater binding affinity towards DNA and BSA.

4. Conclusion

In summary, the ESIPT-based rhodamine-derived sensor **BHS** was successfully developed as a multifunctional colorimetric and fluorescence probe for the selective detection of Cu^{2+} and

OCl^- in aqueous solutions. The sensing mechanism involves the suppression of ESIPT followed by spirolactam ring opening upon analyte interaction, leading to significant absorption and emission shifts. The distinct spectral responses and large Stokes shifts further validate the detection process. Additionally, the **BHS**–Cu^{2+} complex exhibited strong interactions with biomolecules such as ct-DNA and BSA, as demonstrated by fluorescence titration studies and molecular docking simulations. The structural optimization using DFT calculations provides further insights into the binding behavior and electronic properties of the system. The variations in fluorescence of **BHS** caused by Cu^{2+} and OCl^- in biological samples were investigated through the anticancer and biosensing activities of **BHS** in HCT-116 colorectal cancer cells. These findings highlight the potential of **BHS** as an efficient chemosensor for environmental and biological applications, particularly in metal ion and oxidative stress detection.

Data availability

The data supporting this article have been included as part of the ESI.†

Conflicts of interest

There are no conflicts of interest to declare.

Acknowledgements

The authors express their gratitude to Christ University, Bangalore, for providing research facilities, and Center for Research, Christ University for the seed money grant (grant approval number CU-ORS-SM-24/09). Avijit Kumar Das specially acknowledges State University Research Excellence (SERB-SURE) of the Science and Engineering Research Board (SERB) (File Number: SUR/2022/002461) under Anusandhan National Research Foundation (ANRF) and Department of Science and Technology (DST), Government of India, for the financial support by the research grant.

References

1 S.-H. Park, N. Kwon, J.-H. Lee, J. Yoon and I. Shin, *Chem. Soc. Rev.*, 2020, **49**, 143–179.
2 N. Esfandiari and M. Aliofkhazraei, *Talanta*, 2024, **277**, 126365.
3 L. Cui, J. Wu and H. Ju, *Biosens. Bioelectron.*, 2015, **63**, 276–286.
4 K. Sreenivasa Rao, T. Balaji, T. Prasada Rao, Y. Babu and G. R. K. Naidu, *Spectrochim. Acta, Part B*, 2002, **57**, 1333–1338.
5 S. Khan, X. Chen, A. Almahri, E. S. Allehyani, F. A. Alhumaydhi, M. M. Ibrahim and S. Ali, *J. Environ. Chem. Eng.*, 2021, **9**, 106381.
6 R. Sivakumar and N. Y. Lee, *BioChip J.*, 2021, **15**, 216–232.
7 W. Ma, R. Chen, T. Hu, S. Xing, G. Zhou, X. Qin, H. Ren, Z. Zhang, J. Chen and Q. Niu, *Talanta*, 2023, **265**, 124910.
8 R. Chen, S. Xing, T. Hu, Y. Li, J. Chen, Q. Niu and T. Li, *Anal. Chim. Acta*, 2023, **1237**, 340557.
9 P. A. Kim, D. Choe, H. So, S. Park, B. Suh, S. Jeong, K.-T. Kim, C. Kim and R. G. Harrison, *Spectrochim. Acta, Part A*, 2021, **261**, 120059.
10 B. Bansod, T. Kumar, R. Thakur, S. Rana and I. Singh, *Biosens. Bioelectron.*, 2017, **94**, 443–455.
11 Z. Yan, Y. Cai, J. Zhang and Y. Zhao, *Measurement*, 2022, **187**, 110355.
12 F. Abebe, P. Perkins, R. Shaw and S. Tadesse, *J. Mol. Struct.*, 2020, **1205**, 127594.
13 E. Karakuş, *J. Mol. Struct.*, 2021, **1224**, 129037.
14 T. Chopra, S. Sasan, L. Devi, R. Parkesh and K. K. Kapoor, *Coord. Chem. Rev.*, 2022, **470**, 214704.
15 S. Khan, X. Chen, A. Almahri, E. S. Allehyani, F. A. Alhumaydhi, M. M. Ibrahim and S. Ali, *J. Environ. Chem. Eng.*, 2021, **9**, 106381.
16 S. B. Butt and M. Riaz, *J. Liq. Chromatogr. Relat. Technol.*, 2009, **32**, 1045–1064.
17 (*a*) S. Vishnu, A. Nag and A. K. Das, *Anal. Methods*, 2024, **16**, 5263; (*b*) G. C. Das, A. K. Das, D. Das, T. R. Maity, A. Samanta, F. A. Alasmary, A. S. Almalki, A. Iqbal and M. Dolai, *J. Photochem. Photobiol., A*, 2023, **440**, 114663; (*c*) S. Goswami, A. K. Das and S. Maity, *Dalton Trans.*, 2013, **42**, 16259–16263; (*d*) S. Vishnu, S. Maity, A. C. Maity, S. K. Malavika, M. Dolai, A. Nag, Y. bylappa, G. Dutta, B. Mukherjee and A. K. Das, *Spectrochim. Acta, Part A*, 2024, **315**, 124249; (*e*) S. Maity, A. C. Maity, A. K. Das and N. Bhattacharyya, *Anal. Methods*, 2022, **14**, 2739–2744; (*f*) M. S. Kumar, S. Pakrashy, S. Manna, S. M. Choudhury, B. Das, A. Ghosh, A. H. Seikh, M. Dolai and A. K. Das, *Anal. Methods*, 2025, **17**, 2125–2133.
18 (*a*) A. K. Das, Y. Bylappa, A. Nag and M. Dolai, *Anal. Methods*, 2024, **16**, 8164–8178; (*b*) A. K. Das, S. Goswami, C. K. Quah and H. K. Fun, *New J. Chem.*, 2015, **39**, 5669–5675; (*c*) A. K. Das, N. Hayashi, Y. Shiraishi and T. Hirai, *RSC Adv.*, 2017, **7**, 30453–30458; (*d*) A. K. Das, S. Goswami, C. K. Quah and H. K. Fun, *RSC Adv.*, 2016, **6**, 18711–18717; (*e*) A. K. Das, S. Goswami, G. Dutta, S. Maity, T. K. Mandal, K. Khanra and N. Bhattacharyya, *Org. Biomol. Chem.*, 2016, **14**, 570–576; (*f*) A. K. Das, N. Hayashi, Y. Shiraishi and T. Hirai, *RSC Adv.*, 2017, **7**, 30453–30458; (*g*) T. Das, E. Joseph, M. S. Kumar, S. Vishnu, M. Dolai and A. K. Das, *Microchem. J.*, 2024, **199**, 110100; (*h*) M. S. Kumar, M. Dolai, A. Nag, Y. Bylappa and A. K. Das, *Anal. Methods*, 2024, **16**, 676–685.
19 D. Xu, H. Jia, Y. Niu and S. Yin, *Dyes Pigm.*, 2022, **200**, 110185.
20 Y. Wang, X. Wang, W. Ma, R. Lu, W. Zhou and H. Gao, *Chemosensors*, 2022, **10**, 399.
21 S. Sarkar, A. Chatterjee and K. Biswas, *Crit. Rev. Anal. Chem.*, 2024, **54**, 2351–2377.
22 A. Mondal, S. Mukhopadhyay, E. Ahmmed, S. Banerjee, E. Zangrando and P. Chattopadhyay, *J. Phys. Chem. C*, 2020, **124**, 18181–18193.

23 J. Guan, Q. Tu, L. Chen, M.-S. Yuan and J. Wang, *Spectrochim. Acta, Part A*, 2019, **220**, 117114.
24 (*a*) P.-T. Chou, Y.-C. Chen, W.-S. Yu, Y.-H. Chou, C.-Y. Wei and Y.-M. Cheng, *J. Phys. Chem. A*, 2001, **105**, 1731–1740; (*b*) M. T. Ignasiak, C. Houee-Levin, G. Kciuk, B. Marciniak and T. Pedzinski, *Chem. Phys. Chem.*, 2015, **16**, 628–633; (*c*) D. Ghosh, S. Batuta, S. Das, N. A. Begum and D. Mandal, *J. Phys. Chem. B*, 2015, **119**, 5650–5661; (*d*) S. J. Schmidtke, D. F. Underwood and D. A. Blank, *J. Am. Chem. Soc.*, 2004, **126**, 8620–8621; (*e*) M. J. Paterson, M. A. Robb, L. Blancafort and A. D. DeBellis, *J. Am. Chem. Soc.*, 2004, **126**, 2912–2922; (*f*) E. Hadjoudis and I. M. Mavridis, *Chem. Soc. Rev.*, 2004, **33**, 579–588; (*g*) Y. Nakane, T. Takeda, N. Hoshino, K. Sakai and T. Akutagawa, *J. Phys. Chem. A*, 2015, **119**, 6223–6231.
25 P. Majumdar and J. Zhao, *J. Phys. Chem. B*, 2015, **119**, 2384–2394.
26 V. Dujols, F. Ford and A. W. Czarnik, *J. Am. Chem. Soc.*, 1997, **119**, 7386–7387.
27 M. Shortreed, R. Kopelman, M. Kuhn and B. Hoyland, *Anal. Chem.*, 1996, **68**, 1414–1418.
28 H. A. Benesi and J. H. Hildebrand, *J. Am. Chem. Soc.*, 1949, **71**, 2703–2707.
29 Y. Shiraishi, Y. Kohno and T. Hirai, *Ind. Eng. Chem. Res.*, 2005, **44**, 847–851.
30 M. H. Lee, J. S. Kim and J. L. Sessler, *Chem. Soc. Rev.*, 2015, **44**, 4185–4191.
31 R. Bhowmick, A. S. M. Islam, U. Saha, G. Suresh Kumar and M. Ali, *New J. Chem.*, 2018, **42**, 3435–3443.
32 J. C. Stockert, R. W. Horobin, L. L. Colombo and A. Blázquez-Castro, *Acta Histochem.*, 2018, **120**, 159–167; C. Kalaivanan, M. Sankarganesh, M. Y. Suvaikin, G. B. Karthi, S. Gurusamy, R. Subramanian and R. N. Asha, *J. Mol. Liq.*, 2020, **320**, 114423.